FINESSE: Axisymmetric MHD Equilibria with Flow

A. J. C. Beliën,[*,1] M. A. Botchev,[*,2] J. P. Goedbloed,[*]
B. van der Holst,[†] and R. Keppens[*]

[*]*FOM-Institute for Plasma Physics, Association Euratom-FOM, P.O. Box 1207,
3430 BE Nieuwegein, The Netherlands; and* [†]*Centre for Plasma Astrophysics,
K.U. Leuven, Celestijnenlaan 200B, B-3001 Heverlee, Belgium*
E-mail: A.J.C.Belien@siep.shell.com, botchev–goedbloed–keppens@rijnh.nl,
and Bart.vanderHolst@wis.kuleuven.ac.be

The FINESSE code (finite element solver for stationary equilibria) computes axisymmetric magnetohydrodynamic equilibria in poloidal elliptic flow regimes for a variety of astrophysical and laboratory plasma configurations. The obtained equilibria are accurate and are used to study the spectral characteristics of such flowing equilibria. The nonlinear partial differential equation for the poloidal magnetic flux is solved in a weak form via Picard iteration, resulting in a large-scale linear problem. The algebraic Bernoulli equation for the poloidal Alfvén Mach number is solved with a nonlinear root finder. Converged solutions are obtained by iterating on these two equations. © 2002 Elsevier Science (USA)

Key Words: PDEs; finite elements; magnetohydrodynamics; axisymmetric; equilibrium; stellar breeze.

1. INTRODUCTION

For many years the spectrum of waves and instabilities of tokamak fusion plasmas has been studied successfully for static, nonrotating plasmas resulting in optimally shaped plasma cross sections and profiles for fusion operation. However, it has been realized that in present-day tokamaks the notion of static plasmas has to be given up due to common use of neutral beam heating and divertor pumping resulting in substantial toroidal and poloidal plasma rotation.

In astrophysics, the need for the mentioned paradigm shift never occurred; astrophysical plasmas have always been observed as flowing. Nevertheless, stability and wave analysis

---

[1] Presently at Shell International Exploration and Production.

[2] Presently at Math Sciences Faculty, University of Twente, The Netherlands.

of astrophysical plasmas has been performed for static plasmas. On the one hand this is probably due to the success of similar studies in static thermonuclear fusion plasmas, but on the other hand it is likely due to the extreme difficulty in getting meaningful analytic or accurate numerical solutions for flowing plasmas. Such accurate solutions are required to obtain pollution-free spectra and correct stability boundaries.

Magnetohydrodynamic (MHD) equilibria with flow can be, and currently are, obtained by numerical relaxation of the full set of hyperbolic MHD equations toward a stationary state (see, for example, Refs. [14, 17, 20]). However, such computed equilibria generally lack the accuracy to be used as input for spectral studies. Moreover, there is a highly restricted flexibility in determining a priori the kind of solutions that are produced. The advantage of this method is that transonic solutions can easily be obtained (provided the exploited algorithms are shock-capturing).

In this paper we present an algorithm for the solution of the equations governing stationary axisymmetric MHD equilibria that results in very accurate solutions that can be used as starting points for spectral studies. This is far from a trivial extension of the static case. First, there is an additional nonlinear scalar equation, the equivalent of the Bernoulli equation appearing in hydrodynamic flow problems, that determines the density (or poloidal Alfvén Mach number). The nonlinearity of this equation results in four different solution branches: subslow, slow, fast, and superfast. Second, the nonlinear partial differential equation for the poloidal magnetic flux can be either elliptic or hyperbolic, depending on the poloidal Alfvén Mach number.

As far as we know, the first method for the numerical solution of axisymmetric equilibria in elliptic flow regimes was presented and implemented by Żelazny *et al.* [22] for tokamak plasmas. They solved the equilibrium problem by the inverse method and subsequent spectral representation. This involved rewriting and solving the governing equations in flux coordinates instead of using a direct (R, Z) coordinate system. In this paper we present a numerical method based on the direct application of a Galerkin method to solve the partial differential flux equation in combination with nonlinear root finding for the Bernoulli equation. We use isoparametric bicubic Hermite finite elements to discretize the nonlinear partial differential equation, since this has been shown to be quite effective in the equilibrium–spectral code combinations HELENA–CASTOR [12, 13, 15] and CHEASE–MARS [5, 16, 21] for the static case. It permits easy adaptation to different poloidal cross-section geometries and yields quartic convergence behavior that results in accurate solutions already for modest grid resolutions. At the same time, we allow for the presence of an external gravitational field, so that we can generate astrophysically relevant stationary MHD solutions.

This paper is set up as follows. In Section 2, the basic equations of axisymmetric ideal magnetohydrodynamic equilibria with flow are presented and reduced to a core problem in terms of the poloidal magnetic flux function, the squared poloidal Alfvén Mach number, and five arbitrary flux functions. In Section 3, we present and discuss the algorithm to solve the core problem. In Section 4, results are shown for different flow regimes and for different applications to show the abilities of the implemented algorithm. Finally, in Section 5 we draw conclusions.

2. BASIC EQUATIONS AND CORE PROBLEM

In the formulation of the core problem of axisymmetric equilibria with flow, we closely follow the notation and definitions as used by Goedbloed and Lifschitz in their studies of translation symmetric [7] and axisymmetric [9] systems.

The basic equations governing stationary, ideal MHD equilibria are obtained by setting the partial time derivative to zero in the full set of ideal MHD equations. This results in the set of equalities

$$\nabla \cdot (\rho \mathbf{v}) = 0, \tag{1a}$$

$$\rho \nabla \left(\frac{1}{2} v^2 + \frac{\gamma}{\gamma - 1} \rho^{\gamma - 1} S + \Phi_{\text{grav}} \right) - \frac{1}{\gamma - 1} \rho^\gamma \nabla S - \rho \mathbf{v} \times \boldsymbol{\omega} - \mathbf{J} \times \mathbf{B} = 0, \tag{1b}$$

$$\mathbf{v} \cdot \nabla S = 0, \tag{1c}$$

$$\nabla \times (\mathbf{v} \times \mathbf{B}) = 0, \tag{1d}$$

$$\nabla \cdot \mathbf{B} = 0, \tag{1e}$$

which have to hold for the density ρ, velocity $\mathbf{v}$, entropy S, and magnetic field $\mathbf{B}$. In the force balance equation (1b), $\boldsymbol{\omega} \equiv \nabla \times \mathbf{v}$ is the vorticity, and $\mathbf{J} \equiv \nabla \times \mathbf{B}$ is the electric current density (adopting units where the permeability of vacuum $\mu_0 = 1$). The kinetic pressure p is related to the density and entropy by $p \equiv S \rho^\gamma$, where γ is the ratio of specific heats of the plasma. The term Φ_{grav} in the force balance equation (1b) represents the potential of an external gravitational source. Inclusion of this term allows us to study, for example, stellar winds and flows in accretion disks.

The condition of axisymmetry naturally leads to the exploitation of a cylindrical, right-handed coordinate system (R, Z, ϕ). With this choice the divergence-free conditions (1a) and (1e) allow one to write the poloidal components of the velocity and magnetic field in terms of a poloidal stream function χ and a poloidal magnetic flux function ψ, viz.,

$$\mathbf{v} = \frac{1}{\rho R} \mathbf{e}_\phi \times \nabla \chi + v_\phi \mathbf{e}_\phi, \tag{2a}$$

$$\mathbf{B} = \frac{1}{R} \mathbf{e}_\phi \times \nabla \psi + B_\phi \mathbf{e}_\phi. \tag{2b}$$

When substituted into Eq. (1d), the poloidal component shows that

$$\chi = \chi(\psi), \tag{3a}$$

whereas the toroidal component results in

$$\Omega \equiv \frac{1}{R} \left(v_\phi - \frac{\chi' B_\phi}{\rho} \right) = \Omega(\psi). \tag{3b}$$

Similarly, Eq. (1c) yields

$$S = S(\psi), \tag{3c}$$

and the toroidal component of the force balance equation (1b) leads to

$$I \equiv R B_\phi - \chi' R v_\phi = I(\psi). \tag{3d}$$

The component of the force balance equation parallel to the magnetic field results in the definition of another magnetic flux function, i.e., the Bernoulli function [9, 10]:

$$H \equiv \frac{\chi'^2}{2\rho^2}\left(\frac{|\nabla\psi|^2}{R^2}+B_\phi^2\right)-\frac{1}{2}R^2\Omega^2+\frac{\gamma}{\gamma-1}\rho^{\gamma-1}S+\Phi_{\text{grav}}=H(\psi). \tag{3e}$$

Finally, the $\nabla\psi$ component of the force balance equation (1b) results in a partial differential equation for the poloidal magnetic flux, viz.,

$$\nabla\cdot\left[\frac{1-\chi'^2/\rho}{R^2}\nabla\psi\right]+\left(\frac{\chi'}{\rho R^2}+v_\phi B_\phi\right)\chi''+\rho H'-\frac{1}{\gamma-1}\rho\gamma S'+\frac{B_\phi}{R}I'+\rho R v_\phi\Omega'=0, \tag{4}$$

where $' \equiv d/d\psi$. In what follows, we will assume that the gravitational force corresponds to a point source of mass M_{grav} at the origin, hence

$$\Phi_{\text{grav}} \equiv \frac{-GM_{\text{grav}}}{\sqrt{R^2+Z^2}}=-GM_{\text{grav}}g(R,Z), \tag{5}$$

where the spatial dependence of the gravitational potential is denoted by $g(R, Z)$ and G is the gravitational constant.

The core problem of finding stationary axisymmetric MHD equilibria then boils down to specifying the five flux functions, χ, Ω, S, I, H, and solving for ρ and ψ from Eqs. (3e) and (4) subject to boundary conditions.

As shown by Goedbloed and Lifschitz [7, 9], exploiting the poloidal Alfvén Mach number,

$$M^2 \equiv \frac{\rho v_p^2}{B_p^2}=\frac{\chi'^2}{\rho}, \tag{6}$$

instead of the density ρ, and using

$$\Lambda_1 \equiv \chi'^2 H, \quad \Lambda_2 \equiv \frac{\gamma}{\gamma-1}\chi'^{2\gamma}S, \quad \Lambda_3 \equiv \frac{1}{2}\chi'^2\Omega^2, \tag{7a}$$

$$\Lambda_4 \equiv -\frac{I}{\chi'\Omega}, \quad \Lambda_5 \equiv \chi'^2 GM_{\text{grav}}, \tag{7b}$$

instead of the original flux functions, the core problem can be rewritten as

$$\nabla\cdot\left(\frac{1-M^2}{R^2}\right)\nabla\psi = -\frac{1}{M^2}\frac{\partial\Pi_1}{\partial\psi}+\frac{1}{\gamma M^{2\gamma}}\frac{\partial\Pi_2}{\partial\psi}-\frac{1}{1-M^2}\frac{\partial\Pi_3}{\partial\psi}, \tag{8a}$$

$$\frac{|\nabla\psi|^2}{2R^2} = \frac{\Pi_1}{M^4}-\frac{\Pi_2}{M^{2(\gamma+1)}}-\frac{\Pi_3}{(1-M^2)^2}, \tag{8b}$$

where the three generic profiles Π_i $(i = 1, 2, 3)$ are defined in terms of the five flux functions Λ_i $(i = 1, \ldots, 5)$ and an explicit dependence on the coordinates R and Z,

$$\Pi_1 = \Pi_1(\psi; R, Z) \equiv \Lambda_1(\psi)+R^2\Lambda_3(\psi)+\Lambda_5(\psi)g(R,Z)$$
$$= M^2\left(\frac{1}{2}M^2 B^2+\frac{\gamma}{\gamma-1}p\right), \tag{9a}$$

$$\Pi_2 = \Pi_2(\psi) \equiv \Lambda_2(\psi) = \frac{\gamma}{\gamma - 1} p M^{2\gamma}, \tag{9b}$$

$$\Pi_3 = \Pi_3(\psi; R^2) \equiv R^2 \Lambda_3(\psi) \left(1 - \frac{\Lambda_4(\psi)}{R^2}\right)^2 = \frac{B_\phi^2}{2}(1 - M^2)^2. \tag{9c}$$

Note that when the gravitational potential is neglected ($M_{\mathrm{grav}} = 0$) only four flux functions are necessary to specify the problem. Hence, when a solution to Eqs. (8a) and (8b) is found, one has in fact found a solution for a continuous set of original flux functions where one of the functions χ', Ω, S, I, or H can be specified freely. By using the Λ_i flux functions, we easily generate solutions with different density variations by prescribing the flux function χ'^2.

The form of the core problem (8a) and (8b) in terms of the three generic functions Π_i is, besides being compact and esthetically pleasing, also very convenient and well suited for numerical implementation because (i) the singular Alfvénic point $M^2 = 1$ is clearly separated, (ii) a smooth transition to translation symmetric solutions is possible [9], and (iii) given a solution ψ, it makes it possible to view solutions of the Bernoulli equation as functions of three variables only, $M^2 = M^2(P, Q, \Phi)$ (see below). A small drawback of the use of this form of the core equations is that the case of vanishing poloidal flow now requires a nontrivial limit, viz., $\lim_{M^2 \to 0} \Pi_1/M^2 = \lim_{M^2 \to 0} \Pi_2/M^{2\gamma} = \gamma p/(\gamma - 1)$.

The differential operator appearing in (8a) can be elliptic or hyperbolic depending on the value of the squared poloidal Alfvén Mach number M^2 [9, 10, 23]. In this paper, we restrict ourselves to finding solutions in the elliptic flow regimes only. In this way the complicated issues and difficulties with limiting line singularities [9] and boundary conditions are avoided. Furthermore, our solution method is best suited to elliptic problems.

2.1. Poloidal Plasma Cross Sections and Boundary Conditions

In order to deal with a variety of astrophysical and laboratory plasmas, our FINite Element Solver for Stationary Equilibria—FINESSE—has been designed to be very flexible with respect to geometry specification. These geometries are characterized by their poloidal cross sections. Three types of cross sections are currently implemented (see Fig. 1). Together with the boundary conditions they make up three types of applications.
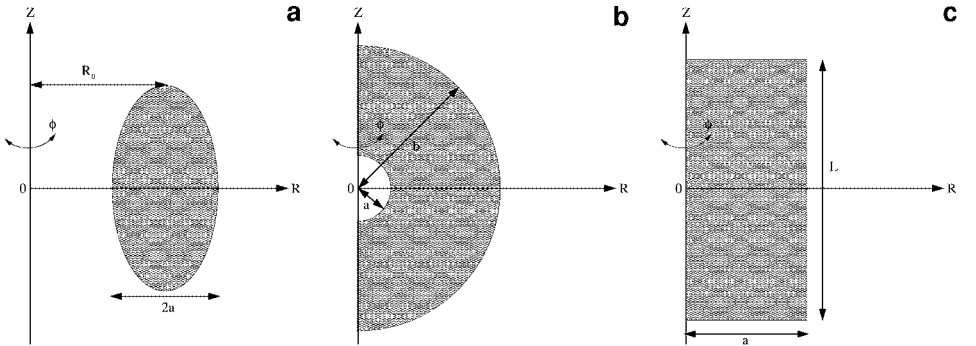

FIG. 1. The different types of poloidal cross sections as implemented in FINESSE. (a) A torus cross section related to applications with nested closed magnetic flux surfaces like tokamak plasmas. (b) An annulus related to stellar wind applications. (c) A flux tube with a predominantly longitudinal magnetic field related to coronal loop applications. The length scale a, as indicated in each frame, is used to make all appearing length variables dimensionless. The cross sections along the z-axis may have arbitrary shape.

2.1.1. *Nested Closed Flux Surfaces: Tokamak Plasmas or Toroidal Flux Tubes in Accretion Disks*

In this case (Fig. 1a), the boundary of the poloidal cross section (R_b, Z_b) is described by

$$R_b(\theta) = R_0 + a r_b(\theta) \cos\theta, \quad Z_b(\theta) = a r_b(\theta) \sin\theta, \quad -\pi \le \theta \le \pi. \quad (10)$$

The major radius of the torus is denoted by R_0 and the minor radius by a. The inverse aspect ratio $\epsilon \equiv a/R_0$ is a geometric quantity measuring the ratio of those two radii. The quantity θ is a polar angle that is measured with respect to the geometric center of the cross section $(R_0, 0)$. The function $r_b(\theta)$ describes the boundary. It is normalized to unity at $\theta = 0$ and $\theta = \pi$.

In this paper we deal with top-down symmetric cross sections: $r(\theta) = r(-\theta)$. However, FINESSE is not limited to such cross sections. The top-down symmetric boundary is specifically modeled as

$$R_b = R_0 + a \cos(\zeta + T \sin\zeta - Q \sin 2\zeta), \quad Z_b = aE \sin\zeta, \quad 0 \le \zeta \le 2\pi, \quad (11)$$

with

$$\theta(\zeta) = \arctan\left(E \frac{\sin\zeta}{\cos(\zeta + T \sin\zeta - Q \sin 2\zeta)}\right) \quad (12)$$

and

$$r_b(\theta(\zeta)) = \sqrt{\cos^2[\zeta + T \sin\zeta - Q \sin 2\zeta] + E^2 \sin^2\zeta}. \quad (13)$$

Here, E measures the ellipticity, T the triangularity, and Q the rectangularity of the cross section.

The imposed boundary conditions are such that the boundary represents a flux surface, i.e., $\psi(R_b, Z_b) = \psi_a$.

2.1.2. *Open and Closed Magnetic Field Lines in a Spherical Annulus: Stellar Wind Plasmas*

A sketch of a typical cross section of this type is shown in Fig. 1b. The two curved "radial" boundaries are represented as

$$R_b^a(\theta) = a r_a(\theta) \cos\theta, \quad Z_b^a(\theta) = a r_a(\theta) \sin\theta, \quad -\frac{\pi}{2} \le \theta \le \frac{\pi}{2}, \quad (14)$$

$$R_b^b(\theta) = b r_b(\theta) \cos\theta, \quad Z_b^b(\theta) = b r_b(\theta) \sin\theta, \quad -\frac{\pi}{2} \le \theta \le \frac{\pi}{2}, \quad (15)$$

where a and b are the small and large "radius," respectively. The angle θ is measured with respect to the R-axis. The functions r_a and r_b are unit profiles normalized to one at $\theta = 0$.

The boundary conditions imposed were chosen to model dipolar magnetic fields. On the symmetry axis $\psi = 0$ is imposed, on the small radial boundary the flux is prescribed, and on the large radial boundary either the flux or the normal derivative of the flux is prescribed.

A top-down symmetric case can be studied as well by considering the range $0 \le \theta \le \pi/2$ and imposing the boundary condition $\partial\psi/\partial Z = 0$ at $\theta = 0$, i.e., on the R-axis.

2.1.3. *Tubelike Geometry: Coronal Loop Plasmas*

The last case models tubelike geometries with a predominantly longitudinal magnetic field. A sketch is shown in Fig. 1c. The radial boundary is specified by

$$R_b(\theta) = ar(\theta), \quad Z_b(\theta) = Z(\theta) \equiv \theta \frac{L}{2\pi}, \quad -\pi \le \theta \le \pi. \tag{16}$$

For uniformity with the other geometries, the longitudinal coordinate Z is expressed in terms of θ. The function $r(\theta)$ is normalized to unity at $\theta = 0$.

As is the case for the nested closed flux surfaces geometry, the radial boundary is considered a flux surface. Hence, the boundary condition is $\psi(R_b, Z_b) = \psi_a$. On the symmetry axis the magnetic flux vanishes and on the two poloidal boundaries either the flux or the normal derivative of the flux is imposed. This flexible setup of the boundary conditions allows us to study many different loop equilibria, for example, with flux that has emerged through the poloidal boundaries. For examples of (static) MHD equilibria in tube geometry, see Beliën *et al.* [1].

2.2. Dimensionless Core Problem

Using a geometric length scale a, a typical density ρ_0, and poloidal magnetic flux value ψ_a, all appearing quantities are made dimensionless. For the case of nested closed magnetic flux surfaces (Fig. 1a), the scaling corresponds to the small radius, the density on the magnetic axis, and the poloidal magnetic flux on the boundary. For the spherical annulus case (Fig. 1b), they are related to the value of the small radius on the equator, to the density on the small radial boundary on the symmetry axis, and to the poloidal magnetic flux at the intersection of the small radial boundary with the equator. Finally, for the tubelike geometry (Fig. 1c) they are related to the tube radius at the midplane (i.e., at $\theta = 0$), to the density on axis at the midplane, and to the flux at the radial boundary.

For nested closed flux surfaces geometries, normalized dimensionless coordinates x and y are then defined as

$$x \equiv \frac{R - R_0}{a}, \quad y \equiv \frac{Z}{a}, \quad \bar{R}(x) \equiv \frac{\epsilon R(x)}{a} = 1 + \epsilon x, \tag{17a}$$

whereas for other geometries they are defined as

$$x \equiv \frac{R}{a}, \quad y \equiv \frac{Z}{a}, \quad \bar{R}(x) \equiv x. \tag{17b}$$

The normalized radial function $\bar{R}(x)$ is introduced as a means of making the core equations uniform for all types of geometries implemented.

The dimensionless normalized poloidal magnetic flux is given by

$$\bar{\psi} = \bar{\psi}(x, y) \equiv \frac{\psi}{\psi_a}. \tag{18}$$

The dimensionless core equations that have to be solved are then given by

$$\bar{\nabla} \cdot \left(\frac{1 - M^2}{\bar{R}^2(x)} \right) \bar{\nabla}\bar{\psi} = -\frac{1}{M^2} \frac{\partial \bar{\Pi}_1}{\partial \bar{\psi}} + \frac{1}{\gamma M^{2\gamma}} \frac{\partial \bar{\Pi}_2}{\partial \bar{\psi}} - \frac{1}{1 - M^2} \frac{\partial \bar{\Pi}_3}{\partial \bar{\psi}}, \tag{19a}$$

$$\frac{|\bar{\nabla}\bar{\psi}|^2}{2\bar{R}^2(x)} = \frac{\bar{\Pi}_1}{M^4} - \frac{\bar{\Pi}_2}{M^{2(\gamma+1)}} - \frac{\bar{\Pi}_3}{(1 - M^2)^2}, \tag{19b}$$

where $\bar{\nabla} \equiv (\partial/\partial x, \partial/\partial y)$, and the dimensionless generic functions

$$\bar{\Pi}_1 \equiv \bar{\Lambda}_1(\bar{\psi}) + \bar{R}^2(x)\bar{\Lambda}_3(\psi) + \bar{\Lambda}_5(\bar{\psi})\bar{g}(x, y) = \left(\frac{a^4}{\psi_a^2}\right)\epsilon^{-2}\Pi_1, \tag{20a}$$

$$\bar{\Pi}_2 \equiv \bar{\Lambda}_2(\bar{\psi}) = \left(\frac{a^4}{\psi_a^2}\right)\epsilon^{-2}\Pi_2, \tag{20b}$$

$$\bar{\Pi}_3 \equiv \bar{R}^2(x)\bar{\Lambda}_3(\bar{\psi})\left(1 - \frac{\bar{\Lambda}_4(\bar{\psi})}{\bar{R}^2(x)}\right)^2 = \left(\frac{a^4}{\psi_a^2}\right)\epsilon^{-2}\Pi_3 \tag{20c}$$

are expressed in terms of the dimensionless flux functions

$$\bar{\Lambda}_1(\bar{\psi}) \equiv \left(\frac{a^4}{\psi_a^2}\right)\epsilon^{-2}\Lambda_1(\psi), \tag{21a}$$

$$\bar{\Lambda}_2(\bar{\psi}) \equiv \left(\frac{a^4}{\psi_a^2}\right)\epsilon^{-2}\Lambda_2(\psi), \tag{21b}$$

$$\bar{\Lambda}_3(\bar{\psi}) \equiv \left(\frac{a^6}{\psi_a^2}\right)\epsilon^{-4}\Lambda_3(\psi), \tag{21c}$$

$$\bar{\Lambda}_4(\bar{\psi}) \equiv \left(\frac{1}{a^2}\right)\epsilon^2\Lambda_4(\psi), \tag{21d}$$

$$\bar{\Lambda}_5(\bar{\psi}) \equiv \left(\frac{a^3}{\psi_a^2}\right)\epsilon^{-1}\Lambda_5(\psi) \tag{21e}$$

and the gravitational potential

$$\bar{g}(x, y) \equiv a\epsilon^{-1}g(R, Z). \tag{21f}$$

The quantity ϵ is the inverse aspect ratio, as mentioned in Section 2.1.1. for nested closed flux surfaces geometries. It is equal to unity for the other geometries.

2.3. Amplitudes and Unit Profile Definitions

The amount of freedom in specifying the flux functions $\bar{\Lambda}_i$ ($i = 1, \ldots, 5$) is infinite and we have to reduce it to a finite number for implementation in FINESSE.

The first step is to separate the degrees of freedom in amplitudes and unit profiles (as was done in, e.g., [6]). We make a slight deviation in this procedure in the sense that, with the exception of A_4, we exploit amplitudes *relative* to $A \equiv A_1$, viz.,

$$\bar{\Lambda}_1(\bar{\psi}) = A\lambda_1(\bar{\psi}), \tag{22a}$$

$$\bar{\Lambda}_2(\bar{\psi}) = AA_2\lambda_2(\bar{\psi}), \tag{22b}$$

$$\bar{\Lambda}_3(\bar{\psi}) = AA_3\lambda_3(\bar{\psi}), \tag{22c}$$

$$\bar{\Lambda}_4(\bar{\psi}) = \epsilon^{-1}A_4\lambda_4(\bar{\psi}), \tag{22d}$$

$$\bar{\Lambda}_5(\bar{\psi}) = AA_5\lambda_5(\bar{\psi}). \tag{22e}$$

The separation in terms of absolute and relative amplitudes is done for two reasons. First, for nested closed flux surface geometries, the amplitude A, which can be factored out of the

right-hand side of Eq. (19a), acts as an eigenvalue determined by the condition that $\bar{\psi} = 0$ on the magnetic axis. For the other geometries A remains a free parameter. Second, the A_i can be related to physically relevant parameters. This second point is discussed in more detail in the Appendix.

In the current implementation of FINESSE the unit profiles $\lambda_i(\bar{\psi})$ ($i = 1, \ldots, 5$) are simply defined as fourth-order polynomials, viz.,

$$\lambda_i = \sum_{j=1}^{5} c_{ij} \bar{\psi}^{j-1}, \quad i = 1, \ldots, 5. \tag{23}$$

The polynomial coefficients, c_{ij}, are constrained by $\max \{\lambda_i(\bar{\psi})\}_{i=1}^{5} = 1$ and

$$\min \lambda_1(\bar{\psi}) > 0, \quad \min \{\lambda_i(\bar{\psi})\}_{i=2,3,5} \geq 0, \quad \min \lambda_4(\bar{\psi}) \geq -1.$$

Note that we allow a sign reversal of the profile λ_4. Through the relation $1 - \Lambda_4/R^2 \propto B_\phi(1 - M^2)$, this signals either a sign reversal in the toroidal magnetic field or a transition from sub-Alfvénic to super-Alfvénic flow. The condition of strictly positive λ_1 is made for convenience so that we are assured of at least one nonzero flux function with a definite sign. The profile amplitudes are constrained by $A > 0$, and $\{A_i\}_{i=2,3,5} \geq 0$ since all flux functions except for Λ_4 are necessarily positive by definition (Eqs. (7a) and (7b)).

From now on we work with dimensionless quantities only and will omit the corresponding bars for convenience.

3. SOLUTION METHOD

Our solution method is guided by the desire to have very accurate solutions that can be used as a starting point for spectral studies. In the spectral formulation, first (magnetic field) and second derivatives (current) of the poloidal magnetic flux appear as well as first derivatives of the poloidal Alfvén Mach number. Since these quantities appear in the potential energy, the accuracy of the potential energy is determined by their accuracies. From spectral studies of static tokamak equilibria it is known that stability of so-called $m = 1$ internal kink perturbations is governed by an expansion of the potential energy to at least fourth-order in the inverse-aspect ratio, ϵ. Therefore, for a correct prediction of (in)stability, the accuracy of the equilibrium quantities has to be such that the potential energy can (in principle) be accurately computed to at least fourth order in the inverse-aspect ratio. This is just a minimal requirement coming from static analysis. For flowing plasmas accuracy requirements might turn out to be even stricter. Typical tokamak aspect ratios of the order $\epsilon \sim 0.1$ indicate that the computed equilibrium quantities should have relative accuracies better than 10^{-4}. Since the convergence of the discretization errors in $\nabla \psi$ and $\nabla^2 \psi$ is generally one and two orders less than for ψ, it indicates that the errors in ψ itself should not exceed 10^{-7}.

Based on the success of the isoparametric bicubic Hermite finite element approach in accurately solving the Grad–Shafranov equation for the static tokamak case and the subsequent transformation to a flux coordinate solution for use in spectral codes (e.g, [12, 13, 15] and [5, 16, 21]), we have opted for a similar approach.

The outer iteration solves for M_i^2 from Eq. (19b) for a *given* converged value $\psi_{;i}$ from the inner iteration. The inner loop uses a simple but effective Picard iteration to find $\psi_{;i}$

from Eq. (19a) for a *given* M_{i-1}^2,

$$\nabla \frac{1 - M_{i-1}^2}{R^2} \nabla \psi_{j+1;i} = -A\Gamma\left(\psi_{j;i}, M_{i-1}^2; x, y\right), \tag{24}$$

where the subscripts i and j denote the outer and inner iteration stages, respectively. The poloidal flux $\psi_{;i}$ denotes the converged solution of the inner Picard iteration corresponding to the ith outer iteration stage. The function Γ is used here as a short notation of the right-hand side of Eq. (19a) normalized to the amplitude, A, of the first flux function Λ_1.

3.1. The Generalized Flux Equation

The linear elliptic partial differential equation (24) for $\psi_{j+1;i}$ is solved numerically with a Galerkin method [19]. The procedure followed is the same as for the solution of the Grad–Shafranov equation that occurs in the formulation of static equilibria [1, 12]. We outline it briefly; details can be found in the above-mentioned references.

A function $\psi(x, y) \in S$ (leaving out the subindices on ψ) is a weak form solution of Eq. (24) when

$$\int_V \frac{1 - M^2}{R^2} \nabla \chi^* \cdot \nabla \psi \, dV = A \int_V \chi^* \Gamma \, dV + \int_{\partial V} \frac{1 - M^2}{R^2} \chi^* \nabla \psi \cdot d\mathbf{S} \tag{25}$$

is true for all test functions $\chi \in T$. The function spaces S and T are the same and consist of functions that have quadratically integrable second derivatives and that satisfy the essential boundary conditions. The plasma volume is denoted V and the bounding surface ∂V. An infinitesimal surface element is represented by $d\mathbf{S}$.

Function space $S(=T)$ is approximated by a finite dimensional subspace $S^{n_r \times n_p}$, of which the bases are spanned by isoparametric bicubic Hermite finite elements covering the poloidal plasma cross section. With bicubic Hermite finite element representations, both ψ and $\nabla \psi$ are continuous across cell boundaries, and convergence of the discretization error is quartic. Isoparametric elements are exploited for their ability to align element cells with the boundary of the physical domain [1, 12, 19]. Within a cell V_k (with subindex k denoting the cell), the poloidal magnetic flux $\psi(x, y)$ then has the isoparametric finite element representation

$$\psi(x(s, t), y(s, t)) = \sum_{l=1}^{4} \sum_{i=1}^{4} H_i(s, t) \psi_{i_{n(k,l)}}, \tag{26}$$

where $(s, t) \in [-1, 1] \times [-1, 1]$ are the local isoparametric coordinates, the Cartesian coordinates are $(x(s, t), y(s, t)) \in V_k$, the functions H_i are the bicubic Hermite elements, and the coefficients $\psi_{i_{n(k,l)}}$ represent function values ($i = 1$), first derivatives $\partial \psi / \partial x$ and $\partial \psi / \partial y$ ($i = 2, 3$), and mixed second derivatives $\partial^2 \psi / \partial x \partial y$ ($i = 4$) at the four corners (subindex l) of a cell (subindex k). The subindex $n = n(k, l)$ denotes the index number of node l of cell k in the list of all nodes.

The discretization of the computational domain is achieved by defining a global "radial" and poloidal coordinate grid in which the boundaries are represented by lines of constant r or θ and by expressing x and y in terms of these coordinates. Nodes (r_i, θ_j) are constructed

by means of monotonic functions of evenly spaced variables (u_i, v_j), viz.,

$$r_i = r(u_i), \quad u_i = \frac{i-1}{n_r - 1}, \quad i = 1, \ldots, n_r \tag{27a}$$

and

$$\theta_j = \theta(v_j), \quad v_j = \frac{j-1}{n_p - 1}, \quad j = 1, \ldots, n_p. \tag{27b}$$

In terms of (x, y) coordinates the nodes of the finite element grid are then given by

$$\left(x_{n(i,j)}, y_{n(i,j)}\right) = (x(r_i, \theta_j), y(r_i, \theta_j)), \quad i = 1, \ldots, n_r, \quad j = 1, \ldots, n_p. \tag{28}$$

By relating the local isoparametric coordinates s and t with the radial coordinates r and θ, respectively, the required isoparametric representation of $x(s, t)$ and $y(s, t)$ can be constructed for each cell.

The condition of a (discretized) weak form solution, Eq. (25), then leads to the matrix problem

$$\mathbf{K} \cdot \mathbf{x}^{(j+1)} = \mathbf{b}^{(j)}, \tag{29}$$

where the components of $\mathbf{x}^{(j+1)}$ are the coefficients ψ_{i_n} and where the superscripts $(j+1)$ and (j) refer to the Picard iteration stage.

The matrix $\mathbf{K}$ is symmetric and positive definite for $M^2 < 1$ or negative definite for $M^2 > 1$, and of order $4n_r n_p$. It has a banded structure with the bandwidth determined by the node ordering of the grid. The implemented node ordering is such that the poloidal directions run fastest and in sequential order. This results in a bandwidth of $4n_p + 7$ for Dirichlet or Neumann poloidal boundary conditions and $8n_p - 1$ for periodic boundary conditions. With a judicious nonsequential ordering of the nodes in the poloidal direction this latter bandwidth can be reduced to $4n_p + 11$.

In the current implementation of FINESSE, Eq. (29) is solved by Cholesky decomposition of the matrix $\mathbf{K}$ and back substitution. For the Picard iteration, the Cholesky decomposition needs to be performed only once at the start.

3.2. The Bernoulli Equation

We solve the Bernoulli equation under the assumption that the poloidal magnetic flux ψ is given as a function of the spatial coordinates x and y. This turns the Bernoulli equation (19b) into a nonlinear algebraic equation for the poloidal Alfvén Mach number M^2.

With the definitions

$$X \equiv \frac{1}{M^2} \tag{30}$$

and

$$P \equiv \frac{\Pi_2}{\Pi_1}, \quad Q \equiv \frac{\Pi_3}{\Pi_1}, \quad \Phi \equiv \frac{|\nabla\psi|^2}{2R\Pi_1}, \tag{31}$$

we recast the problem of finding solutions of the Bernoulli equation into finding the roots of $B_\gamma(X; P, Q, \Phi) = 0$, where

$$B_\gamma(X; P, Q, \Phi) \equiv X^2 - PX^{\gamma+1} - Q\frac{X^2}{(X-1)^2} - \Phi. \tag{32}$$

This representation is concise and very convenient for analysis and numerical implementation.

In general, when certain solvability constraints are met (see below) by the parameters P, Q, and Φ, four real, nonnegative zeros of B can be found, viz.,

$$B_\gamma(X; P, Q, \Phi) = 0 \Rightarrow X = X_{0,1,2,3}(P, Q, \Phi; \gamma). \tag{33}$$

From elementary algebra it follows that

$$0 \equiv \underbrace{X_0^b \le X_0 \le X_1 \le X_1^b}_{\text{fast}} \le 1 - \sqrt{Q} \tag{34a}$$

and

$$1 + \sqrt{Q} \le \underbrace{X_2^b \le X_2 \le X_3 \le X_3^b}_{\text{slow}} \le P^{-1/(\gamma-1)}, \tag{34b}$$

where $X_{0,1,2,3}^b \equiv X_{0,1,2,3}(P, Q, \Phi = 0; \gamma)$ are the Bernoulli flow boundaries. The solutions with $X < 1$ $(X > 1)$ represent fast (slow)-flow solutions. When Q is nonzero a region around the Alfvén point, $X_A \equiv 1$, is inaccessible.

We will use a Van Wijngaarden–Dekker–Brent nonlinear root finder [18]. Roots have to be bracketed for this root finder. Hence, we need to find a bracket between X_0 and X_1 and one between X_2 and X_3. Fortunately, these brackets are easily available and are physically significant. The fast X_f and slow X_s hyperbolic transition points act like brackets. These two transition points are given by the zeros of the function (see [7, 9])

$$V_\gamma(X; P, Q) \equiv (X - 1)\left(1 - \frac{1}{2}(\gamma + 1)PX^{\gamma-1}\right) + \frac{Q}{(X-1)^2}. \tag{35}$$

For general solutions, i.e., $\Phi \ge 0$, the following orderings hold:

$$0 = X_0^b \le X_0 \le X_f, \quad X_f \le X_1 \le X_1^b \le 1 - \sqrt{Q}, \tag{36a}$$

$$1 + \sqrt{Q} \le X_2^b \le X_2 \le X_s, \quad X_s \le X_3 \le X_3^b \le P^{-1/(\gamma-1)}. \tag{36b}$$

The lower and upper bounds are used as brackets in the nonlinear root-finding procedure.

As mentioned above, solvability conditions have to be met in order to have real solutions of the Bernoulli equation. For the fast flow regime they are

$$Q \le 1 \quad \text{and} \quad \Phi \le X_f^2 - PX_f^{\gamma+1} - Q\frac{X_f^2}{(X_f - 1)^2}. \tag{37a}$$
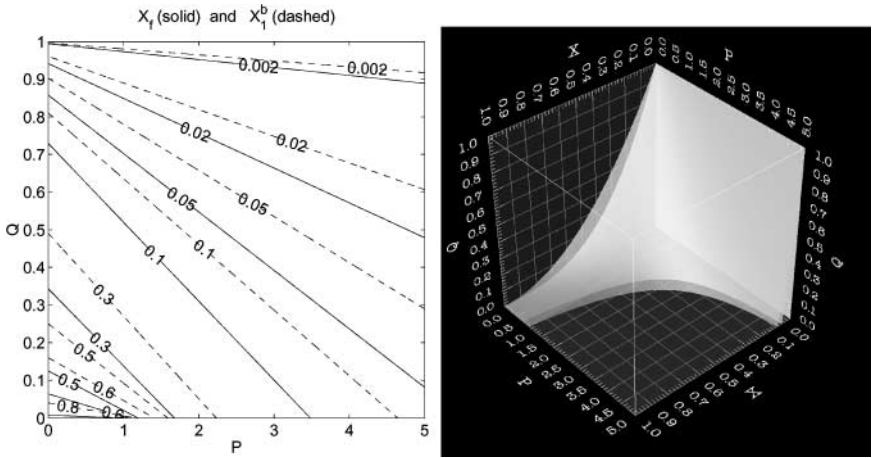
FIG. 2. The Bernoulli boundary X_0^b (the plane $X = 0$) and X_1^b and the transition from ellipticity to hyperbolicity X_f for the fast-flow regime, as contour plots (left) and surface plots (right).

For the slow flow regime they are

$$P \le P^\dagger(Q) \le 1 \quad \text{and} \quad \Phi \le X_s^2 - PX_s^{\gamma+1} - Q\frac{X_s^2}{(X_s - 1)^2}. \tag{37b}$$

The definition of $P^\dagger(Q)$ is somewhat involved. It can be found in Ref. [9]. In the same reference, it is shown that the solution X_0 corresponds to a fast hyperbolic stationary flow state, X_1 is in a fast elliptic flow regime, X_2 corresponds to a slow elliptic flow region, while X_3 is slow hyperbolic when $X_3 \le X_c$ and subslow elliptic otherwise. The latter X_c is defined by $M^2 = M_c^2 = \gamma p/(\gamma p + B^2)$.

The Bernoulli boundaries $X_{0,1,2,3}^b$ and the fast and slow hyperbolic transition points X_f and X_s are *fundamental* functions of two variables, P and Q, with a parametric dependence on the ratio of specific heats γ as the only physical parameter entering. In Figs. 2 and 3
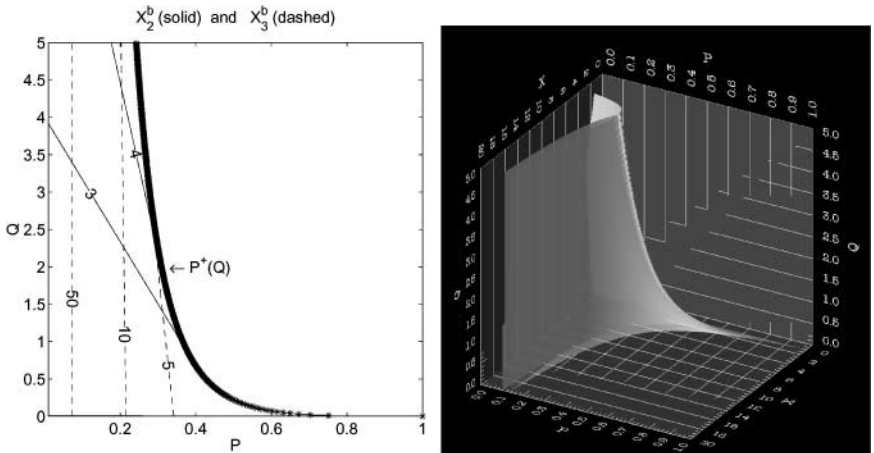

FIG. 3. The Bernoulli boundary X_2^b and X_3^b for the slow-flow regime, as contour plots (left) and surface plots (right). The surfaces join at the curve $P^\dagger(Q)$ depicted in the left panel.

we plotted the Bernoulli boundaries taking $\gamma = 5/3$. Figure 2 is relevant for the fast-flow regime, since all possible fast solutions X_1 are located between the two surfaces X_1^b and X_f. Figure 3 is of interest for the slow-flow regime, showing the Bernoulli boundaries X_2^b and X_3^b. These surfaces collapse onto the curve $P^\dagger(Q)$ depicted in the left panel. The hyperbolic transition surface, X_s, is not shown since it is located very close to the X_3^b surface and it would render them indistinguishable.

3.3. Convergence Characteristics

In this section, we study the convergence properties of the numerical method. We investigate both the convergence toward a single solution via the inner and outer iteration loops and the convergence of the finite element discretization errors.

The convergence of the solution in the inner and outer iteration loops is determined by the max–norm of the iteration variations. The max–norm is defined by

$$\|f\| = \max_{i_n=1,\ldots,n} \left| f\left(x_{i_n}, y_{i_n}\right) \right|, \tag{38}$$

where i_n runs over all nodes of the finite element grid.

In Figs. 4 and 5, the convergence history of the solution in the inner and outer iteration loops is plotted for equilibrium Case T3 (left) and Case T4 (right) (see Table II). The acceptance criterium for the inner (Picard) iteration is that the max–norm of the variation is smaller than 10^{-8}. As soon as this criterion is met, a new outer iteration is started that is visible in Fig. 4 as a sudden jump. The acceptance criterium for the outer loop is that the max–norms of the variations of both ψ and M^2 are smaller than 10^{-8}.

The following observations can be made from Figs. 4 and 5. First, the convergence of the inner and outer iteration is exponential, as indicated by the nearly straight lines in the log-linear plots. This is an excellent property of our numerical algorithm. Second, the number of iterations necessary to obtain a converged inner solution decreases as the outer solutions
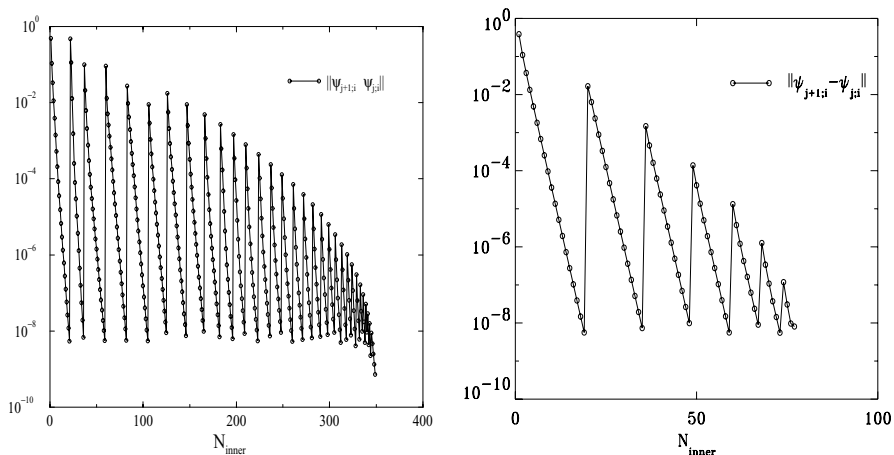

FIG. 4. Convergence history of two solutions from Table II in the inner iteration loop with $n_r = n_p = 17$. (Left panel) A typical slow-flow solution (Case T3). (Right panel) A fast elliptic solution (Case T4). The inner iteration is accepted as converged when $\|\psi_{j+1;i} - \psi_{j;i}\| \leq 10^{-8}$. Each jump indicates a new outer iteration stage.
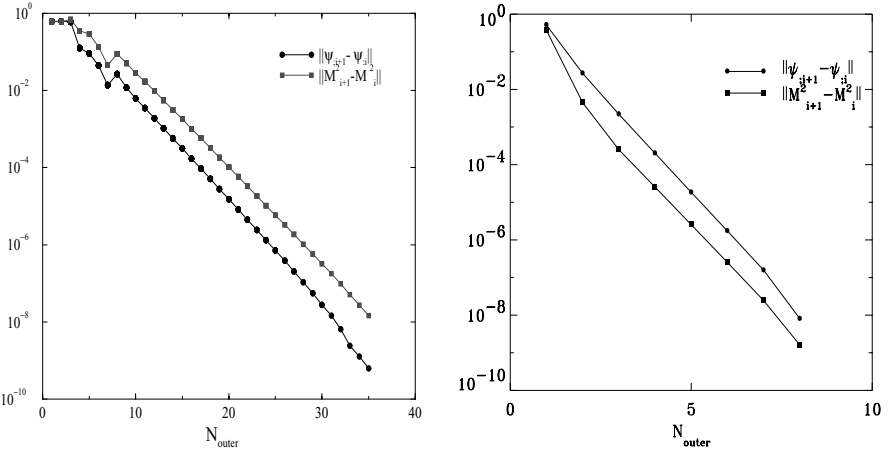
FIG. 5. Convergence history of two solutions in the outer iteration loop for the same slow-flow (left) and fast-flow (right) solution as in Fig. 4. The outer iteration, and hence the final solution, is accepted as converged when $\|\psi_{;i+1} - \psi_{;i}\| \leq 10^{-8}$ and $\|M_{i+1}^2 - M_i^2\| \leq 10^{-8}$.

get closer to convergence (e.g., from 21 in the first outer iteration to 1 in the last one for Case T3). It should be noted that the overall convergence behavior of the method, as shown in Figs. 4 and 5, is (almost) insensitive to the spatial resolution.

Computationally, the most expensive part of the solution algorithm is the Cholesky decomposition of matrix **K** every time a new outer iteration is started. From Fig. 4 it is then clear that the later stages in the outer iteration become relatively more and more expensive, since the number of inner iterations reduces greatly. Therefore, the computational cost of our method might be improved by the use of an iterative linear algebra solver and good preconditioner, for example an LU-decomposition of the matrix **K** obtained at the start. A hybrid method where an iterative linear algebra solver was switched on only when the
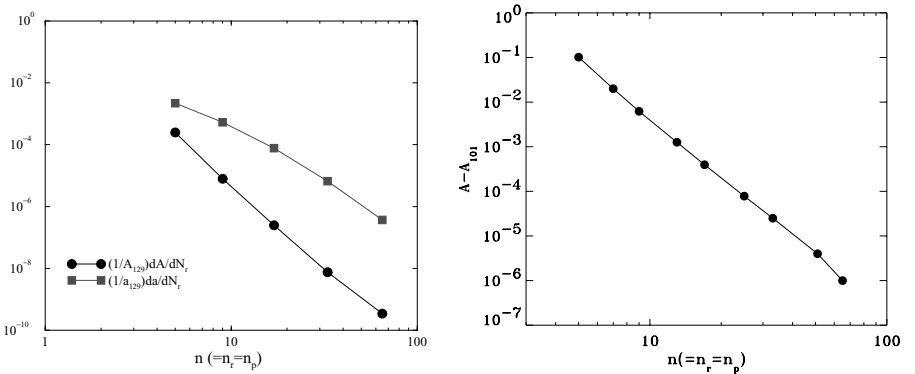

FIG. 6. (Left panel) The convergence rate of the discretization error of the eigenvalue $A_n = A_\infty + Cn^{-\alpha}$ and the value of $a_n = a_\infty + Dn^{-\beta}$ ($a = \partial^2\psi/\partial x^2$) at the magnetic axis for equilibrium (Case T3). The centered difference of these quantities is plotted. The slopes at $n = 65$ are approximately -5 and -4, respectively, indicating $\alpha = 4$ and $\beta = 3$. (Right panel) Similarly for fast flow (Case T4), quartic convergence is visible by plotting $A_n - A_{101}$ for increasing n.

TABLE I
**CPU Timings for Cases T3 (on SGI Origin 200) and T4 (on SGI Octane2)
from Table II for Varying Spatial Resolutions**

Case	CPU	$n = n_r = n_p$	Time (s)
T3	270 Mhz IP27 MIPS R12000	5	8.626
		9	12.878
		17	43.438
		33	212.223
		65	1483.075
T4	360 Mhz IP30 MIPS R12000	7	3.957
		13	6.282
		25	19.611
		51	143.544
		101	871.050

number of inner iterations had dropped below some threshold might reduce costs even further. Since the relative cost of the nonlinear root-finding procedure to solve the Bernoulli equation will increase for these methods, the use of database interpolation that has been developed and implemented as well [2] might be an interesting option for further cost reduction.

The convergence properties of the solutions for increasing spatial resolution, as measured by the number of radial and poloidal nodes indicated by $n = n_r = n_p$, is demonstrated in Fig. 6. For both a slow (Case T3) and a fast (Case T4) solution, we confirm the expected quartic convergence behavior through the use of bicubic Hermite finite elements. This is done as follows. To quantify the order of the discretization error in ψ, we use the eigenvalue A appearing in the equilibrium calculation of geometries with nested closed flux surfaces. Assuming $A_n = A_\infty + Cn^{-\alpha}$, with n the number of radial and poloidal nodes and A_∞ the exact value, the convergence rate α can easily be obtained by plotting dA_n/dn versus n in a log–log plot. This is shown in the left panel of Fig. 6 for Case T3. From this figure it follows that $\alpha = 4$. Hence, we find the same quartic convergence as in the bicubic finite element methods exploited to solve static equilibria [1, 12]. In Fig. 6, we have also plotted the convergence of $\partial^2\psi/\partial x^2$ on the magnetic axis. Its convergence rate is cubic. In the right panel of Fig. 6, we plot the deviation $A_n - A_{101}$ for several runs of the fast-flow Case T4, again clearly showing quartic convergence. For completeness, Table I indicates CPU timing results for several spatial resolutions. From Figs. 4–6 and Table I, we conclude that our solution method delivers very accurate stationary MHD equilibria within seconds to several minutes.

4. TYPICAL SOLUTIONS

In this section we show several equilibrium solutions, as computed by FINESSE, for different geometries and different flow regimes. The magnetic configurations include tokamak-relevant geometries with nested, closed flux surfaces, as well as astrophysical applications with nested and open flux surfaces. First, we give five examples with nested flux surfaces, with plasma flows ranging from subslow, to slow, to fast regimes, without and with external

TABLE II
Specification of the Input Amplitudes and Unit Profiles for All Equilibria

Case	A^a, λ_1	A_2, λ_2	A_3, λ_3	A_4, λ_4	A_5, λ_5
T1—subslow	8.26×10^{-4}	0.002	4×10^{-4}	3400	0
$\epsilon = 0.05$	$1 - 1.8\psi + 0.9\psi^2$	$1 - 1.9\psi + 0.95\psi^2$	1	1	$1 - 0.95\psi$
T2—slow	0.142	0.001	1×10^{-4}	500	0
$\epsilon = 0.05$	$1 - 0.4\psi + 0.2\psi^2$	$1 - 1.6\psi + 0.8\psi^2$	1	1	$1 - 0.95\psi$
T3—slow	1.03	0.1	5×10^{-9}	350	0
$\epsilon = 0.3$	$1 - 1.8\psi + 0.9\psi^2$	$1 - 1.8\psi + 0.9\psi^2$	1	1	$1 - 0.95\psi^2$
T4—fast	84.5	0.1	5×10^{-9}	1750	0
$\epsilon = 0.3$	1	$1 - 1.8\psi + 0.9\psi^2$	1	1	$1 - 0.95\psi^2$
AD—slow	0.267	0.001	1×10^{-4}	500	1
$\epsilon = 0.05$	$1 - 0.4\psi + 0.2\psi^2$	$1 - 1.6\psi + 0.8\psi^2$	1	1	$1 - 0.49\psi^2$
SB—subslow	5×10^{-8}	0.1	1×10^{-7}	10^6	1
$a/b = 0.2$	1	1	1	ψ	1

^{a} Output value for the nested geometries.

gravitational field, for either circular or disklike cross sections. Our final example represents a stellar breeze for an annular cross-section geometry where gravity plays a role. These solutions have been obtained for specific choices for amplitudes A_i and unit profiles λ_i, as listed in Table II. In the Appendix, we relate these choices with physically relevant parameters. If not stated otherwise, the ratio of specific heats $\gamma = 5/3$.

4.1. Nested Magnetic Configurations

4.1.1. *Tokamak Plasmas: Near-Static Flow Equilibrium*

Our first example is a subslow equilibrium for a tokamak (T1) with a circular cross section, where the inverse aspect ratio is $\epsilon = 0.05$. Figure 7 shows the computed equilibrium as contour plots of the squared poloidal Alfvén Mach number M^2, the density ρ, the toroidal magnetic field component B_ϕ, the ratio M^2/M_c^2 with $M_c^2 = \gamma p/(\gamma p + B^2)$, the pressure p, and the toroidal velocity component v_ϕ. All contour plots are superposed on a straight field line coordinate grid (ψ, ϑ) where ϑ is a poloidal angle constructed in such a way that the equilibrium magnetic field is straight on each magnetic surface, $(d\phi/d\vartheta)_{\text{fieldline}} = \mathbf{B} \cdot \nabla\phi/\mathbf{B} \cdot \nabla\vartheta = J B_\phi/R = q(\psi)$, where J is the Jacobian of the (ψ, ϑ, ϕ) coordinate system, and q denotes the safety factor. This coordinate transformation involves computing the inverse solution, $x(\psi, \vartheta)$, $y(\psi, \vartheta)$, as well as constructing the straight field line coordinate ϑ. This is done via exact root finding and interpolation of the finite element solution ψ. The use of these straight field line coordinates (ψ, ϑ) is only needed for subsequent spectral studies, where a proper representation of dynamics perpendicular and parallel to the magnetic field is crucial.

As can be seen from Fig. 7 $M^2 \ll 1$ and $M^2 < M_c^2$, so the equilibrium is a near-static, subslow elliptic flow equilibrium far away from the transition to hyperbolic flow. Since it is near-static, the pressure is roughly a flux function $p \sim p(\psi)$ (recall that for static equilibria $p = p(\psi)$). The $q(\psi)$ profile, shown in Fig. 8, reveals that this equilibrium is representative for a realistic flowing tokamak plasma: $q(\psi = 0) \simeq 1$ with an increase toward the edge.
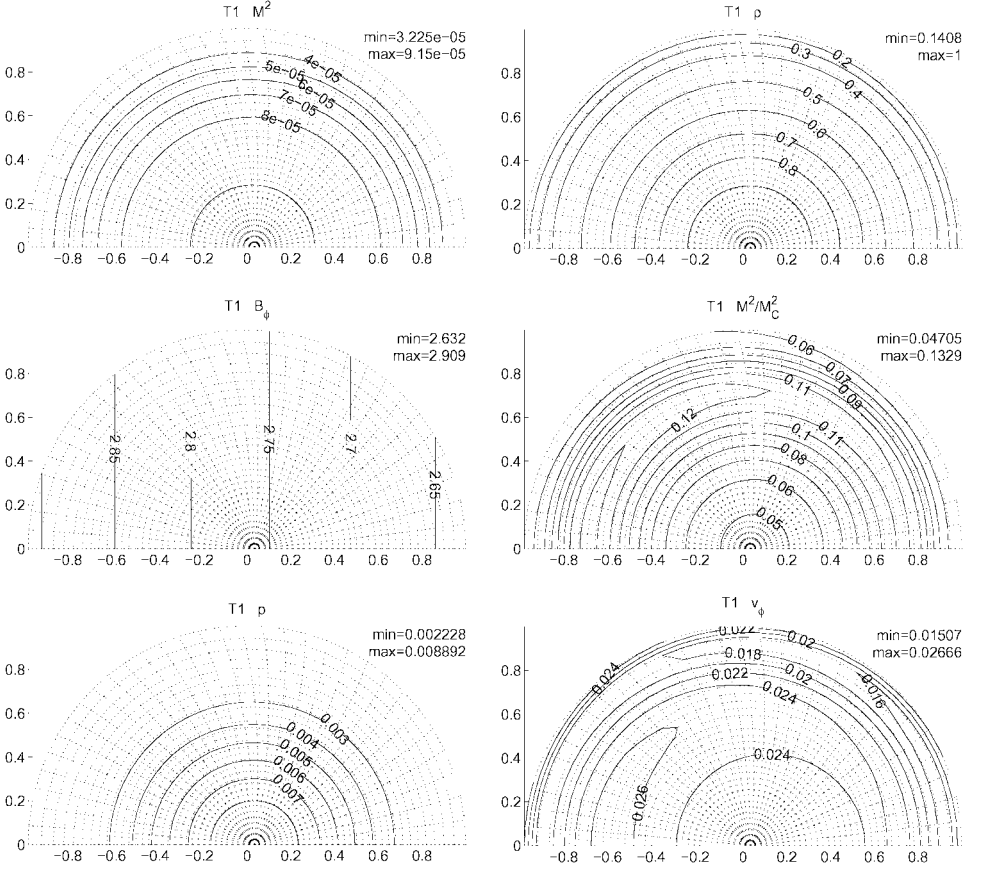
FIG. 7. The subslow-flow tokamak equilibrium T1. The plots from left to right and from top to bottom show, respectively, the squared poloidal Alfvén Mach number M^2, the density ρ, the toroidal magnetic field component B_ϕ, the ratio M^2/M_c^2, the pressure p, and the toroidal velocity component v_ϕ. The dotted lines correspond to a straight field line (ψ, ϑ)-coordinate grid.

The plasma beta is $\beta \equiv 2\langle p\rangle/(B_\phi^2|_{\psi=0}) = 9.63 \times 10^{-4}$. With $\beta \sim \mathcal{O}(\epsilon^2)$, this tokamak equilibrium is low beta. The toroidal field component has a clear $1/R$ dependence, making RB_ϕ nearly a flux function, which holds exactly in the static case. Since gravity is absent, we can freely prescribe the flux dependence of χ'^2. The density plot from Fig. 7 assumed $\chi'^2 = 1 - 0.95\psi$.

For this near-static equilibrium, it can be seen from the figure that M^2 behaves almost like a flux function. In the Appendix, we explain why this behavior applies to all near-static equilibria. The velocity field $\mathbf{v}$ can generally be written as

$$\mathbf{v} = \frac{M}{\sqrt{\rho}}\mathbf{B} + \Omega R\mathbf{e}_\phi, \tag{39}$$

which decomposes the flow into a part parallel to the magnetic field and a nonparallel part of the toroidal velocity. For the near-static $M^2 \ll 1$ case, the toroidal velocity v_ϕ is essentially given by ΩR. From the figure, we conclude that $\Omega \sim \mathcal{O}(\epsilon^2)$, which is a familiar result for a low-beta tokamak plasma [11].
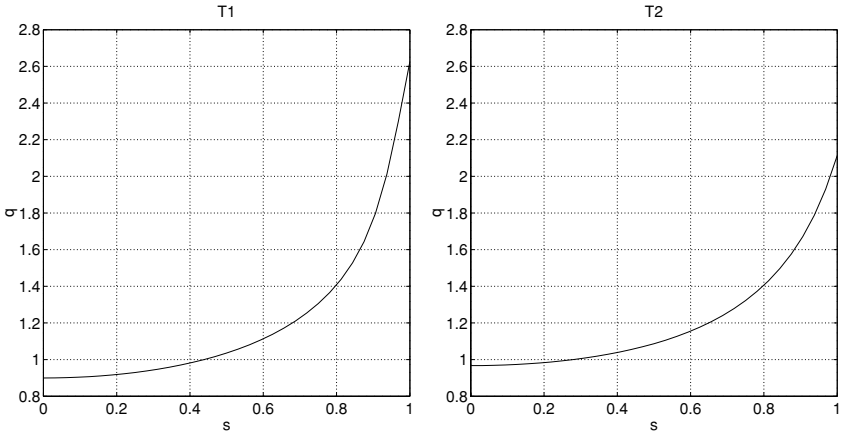
FIG. 8. The q-profiles for the tokamak-relevant equilibria T1 (left) and T2 (right).

4.1.2. *Tokamak Plasmas: Slow Flow Equilibrium*

We now present equilibrium T2, where the flow is completely in the slow elliptic regime (Fig. 9), for the same geometry as in the first example. This is a slow-flow solution, as can be seen immediately from the extremal values of M^2 and M^2/M_c^2 reported on the plots:
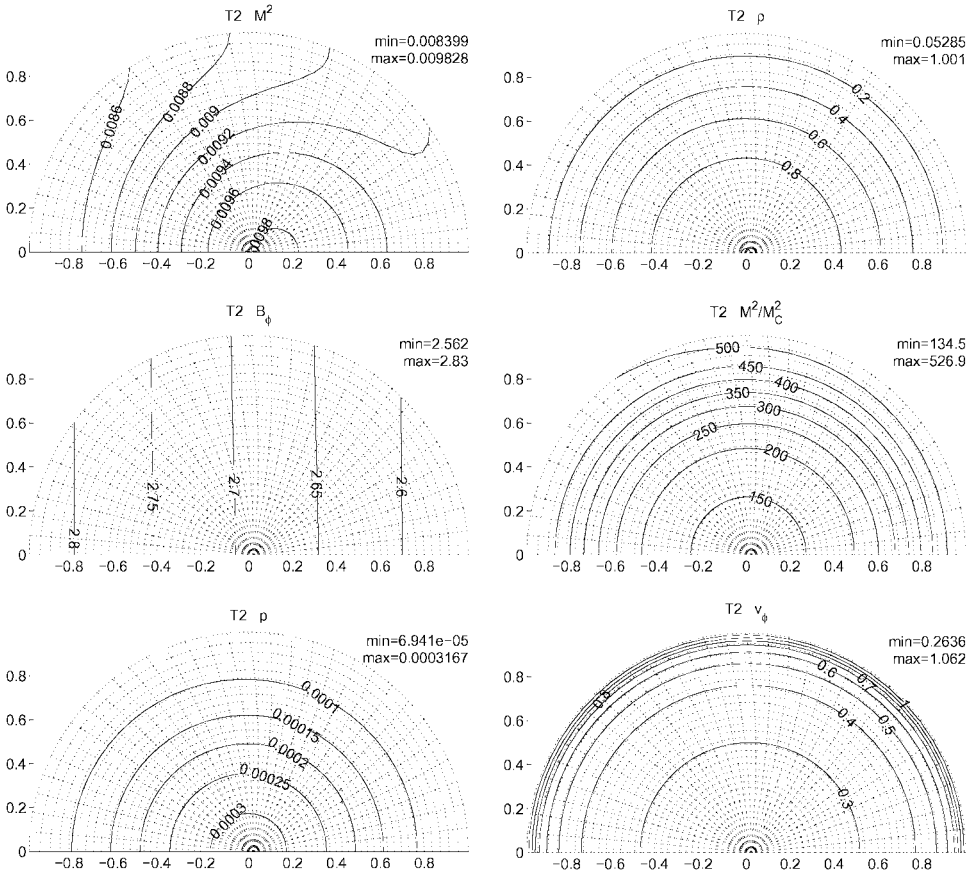

FIG. 9. As in Fig. 7, the slow-flow tokamak equilibrium T2.

$M_c^2 < M^2 < 1$. An important notable difference from the subslow tokamak equilibrium presented in the previous example is that M^2 is clearly not a flux function anymore. Notice the outward shift of the contour lines of M^2 with respect to the flux coordinate grid. This equilibrium still has a fusion-relevant q-profile (Fig. 8) and the familiar $\sim 1/R$ variation in B_ϕ. However, with a plasma beta value of $\beta = 4.06 \times 10^{-5}$ the equilibrium is more a balance between the Lorentz and the centrifugal force in the poloidal cross section. The nonnegligible flow causes noticeable misalignment between the contour lines of p and the flux surfaces. Again, as in the first example, the density is computed based on a chosen $\chi'^2 = 1 - 0.95\psi$. The difference between this slow equilibrium and the subslow equilibrium in the previous example clearly manifests itself in the toroidal velocity v_ϕ: it is two orders of magnitude larger for this equilibrium and it varies more significantly (notice the difference in max v_ϕ/ min v_ϕ).

Using the straight field line representation of the obtained slow-flow equilibrium (shown as the dotted lines in Fig. 9), we now demonstrate that the obtained accuracy in the equilibrium solution is clearly sufficient to calculate the entire ideal continuous spectrum of all MHD waves and instabilities localized to individual flux surfaces. Using the companion spectral code PHOENIX [3] we solve the linearized ideal MHD equations, from which we obtain a spectrum of (complex) eigenvalues λ. When the ideal continuous spectrum is calculated, the variation of the normal modes with time dependence $e^{\lambda t}$ in the direction across the flux surfaces is known a priori and prescribed in PHOENIX. Since the equilibrium is axisymmetric, a single toroidal Fourier mode $e^{in\phi}$ can be selected. For the analysis of the modes localized on single flux surfaces, labeled by $s \equiv \sqrt{\psi}$, the poloidal variation is represented as a truncated Fourier series $\sum e^{im\vartheta}$. The result of such an analysis for $n = -1$, and m values ranging from -6 to 2, is plotted in Fig. 10. The influence of the FINESSE grid resolution on the eigenmodes calculated by PHOENIX is also shown. For each resolution, we interpolated the equilibrium solution to a straight field line coordinate grid of size 129×129. A rigorous analysis of all occurring wave modes and the numerous mode couplings visible as either avoided crossings or mergers of normal mode branches is presented elsewhere. Due to the presence of flow in the tokamak equilibrium, it turns out that for each poloidal m mode, a quintet of branches can be identified corresponding to flow-advected entropy disturbances and two pairs of forward- and backward-traveling singular wave modes, namely a slow and an Alfvén wave pair.

4.1.3. *Plasmas with Large Poloidal Flow*

The tokamak-relevant examples given above had low poloidal Alfvén Mach numbers M, with values ranging up to 0.01 for the near-static (subslow) Case T1 and up to 0.1 for the slow Case T2. However, FINESSE can also calculate stationary plasma states with significant background flow $M \sim \mathcal{O}(1)$, and this is shown in the following two examples. For the sake of comparison, we keep the circular shape of the toroidal cross section. The effect of toroidicity is amplified by raising the aspect ratio by a factor of 6 to $\epsilon = 0.3$.

Slow-flow equilibrium. As in the tokamak Case T2 from Fig. 9, the equilibrium T3 in Fig. 11 is still a slow elliptic flow equilibrium. The increased aspect ratio causes a marked outward shift of the flux surfaces, as a combined effect of toroidicity (Shafranov shift) and centrifugal forces. This equilibrium has a predominantly poloidal magnetic field, with a corresponding q-profile which would increase from 0.03 on the magnetic axis to 0.1 at
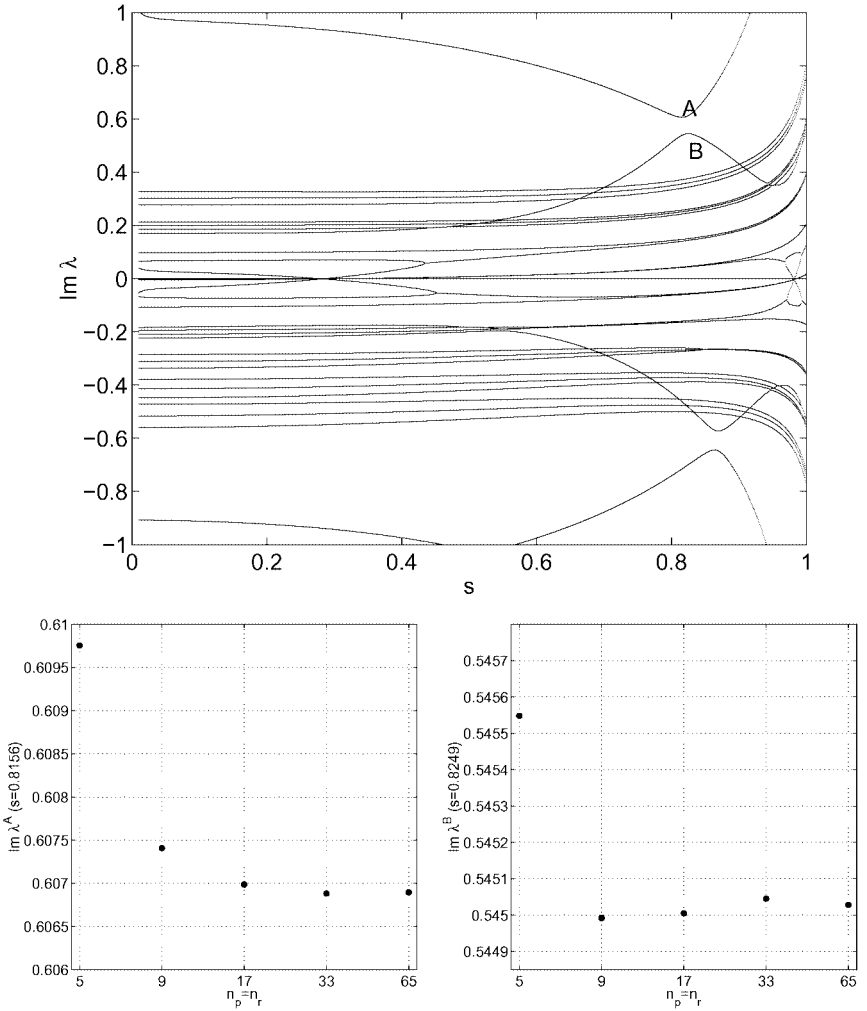
FIG. 10. An examplary spectral analysis of the slow-flow equilibrium shown in Fig. 9. (Top) The oscillation frequencies Imλ of the ideal MHD eigenmodes localized to individual flux surfaces labeled $s = \sqrt{\psi}$ trace out quintets of normal mode branches for each poloidal mode number m. Avoided crossings (e.g., creating the gap bordered by modes labeled A and B) and mergers of these curves signal intricate poloidal mode couplings. (Bottom) The convergence of the individual eigenfrequencies A (left) and B (right) as a function of the equilibrium resolution.

the edge. Notice the major difference in the toroidal field component with respect to the T2 equilibrium: the $\sim 1/R$ dependence has now disappeared. Also, the toroidal velocity v_ϕ varies yet more significantly, having a pronounced local minimum at an intermediate flux surface. A high plasma beta value, $\beta = 0.0201$, for this equilibrium suggests larger, compared to the T2 equilibrium, values of $M_c^2 \approx \frac{1}{2}\gamma\beta$. This is indeed the case, as can be seen from the M^2/M_c^2 values.

Fast-flow equilibrium. In Fig. 12, a fast elliptic flow equilibrium T4 is presented. A strong toroidal flow, i.e., large values of v_ϕ, leads to an equilibrium that has almost nothing in common with tokamaklike equilibria T1 and T2. This is a high-beta configuration: $\beta = 0.0139$. Compared to the T3 equilibrium, there is a yet stronger centrifugally driven displacement of the flux surfaces: notice the significant outward shift of the magnetic axis.
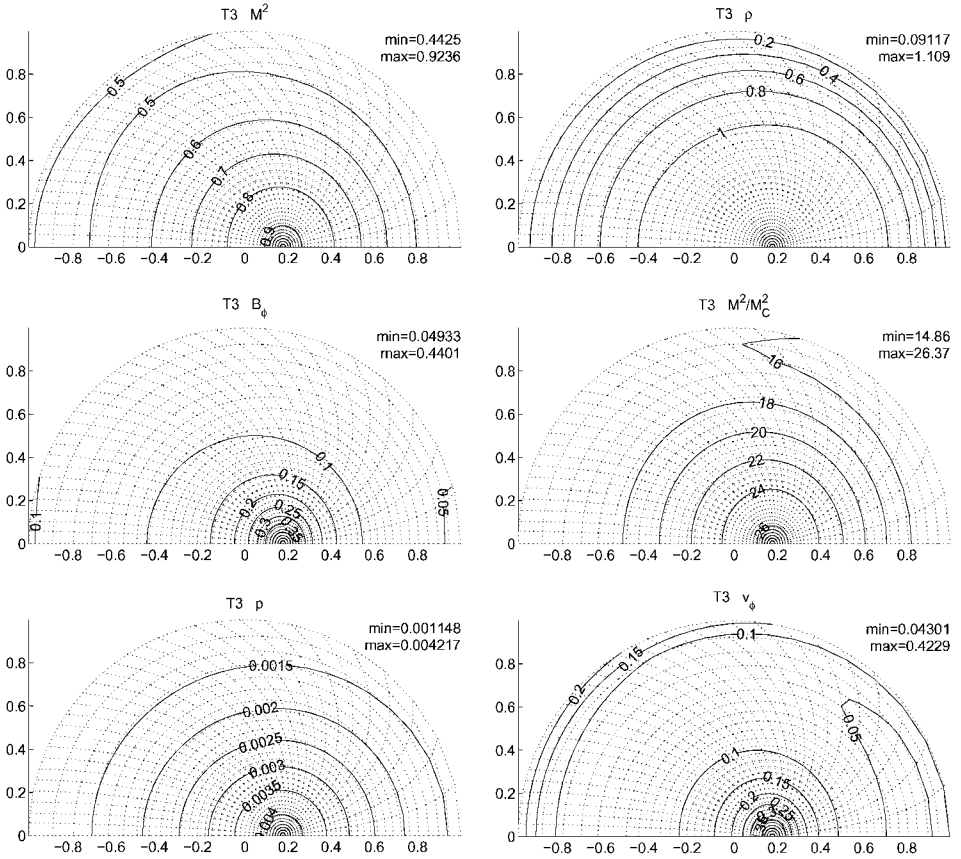
FIG. 11. As in Figs. 7 and 9, for the slow elliptic T3 equilibrium.

The density distribution is even more shifted toward the outer edge, which is mimicked by the pressure variation in such a way that the entropy ends up in accord with its prescribed flux dependence.

4.1.4. *Flux Tori in Accretion Disks*

The previous examples did not include the influence of gravity. As an idealized model for a magnetized accretion disk (or a flux loop in such a disk) about a compact stellar object, we now calculate a slow elliptic flow solution (AD in Table II) in a flattened disk. The disk geometry is assumed to be top-down symmetric and has an aspect ratio of $\epsilon = 0.05$ with an ellipticity of $E = 0.5$. The solution is shown in Fig. 13. The gravitational point source, to the left of the plots, clearly influences the density distribution in the disk, whose maximum is displaced inward with respect to the magnetic axis. Compared to the slow equilibrium T2, where centrifugal and magnetic forces were dominant (negligible thermal pressure effects), this configuration is now a careful balance between the central inward gravitational force and centrifugal and magnetic forces. Indeed, the toroidal velocity turns out to be roughly twice the local Keplerian velocity, while the plasma β is 2.7×10^{-5}. The strength of the gravitational field as characterized by the ratio of the escape speed $v_{\mathrm{esc}} = \sqrt{2GM_{\mathrm{grav}}/R}$ to the local adiabatic sound speed $c_s = \sqrt{\gamma p/\rho}$ is about 13 at the magnetic axis and reaches up to 22 at both edges of the disk. As the spectral companion code
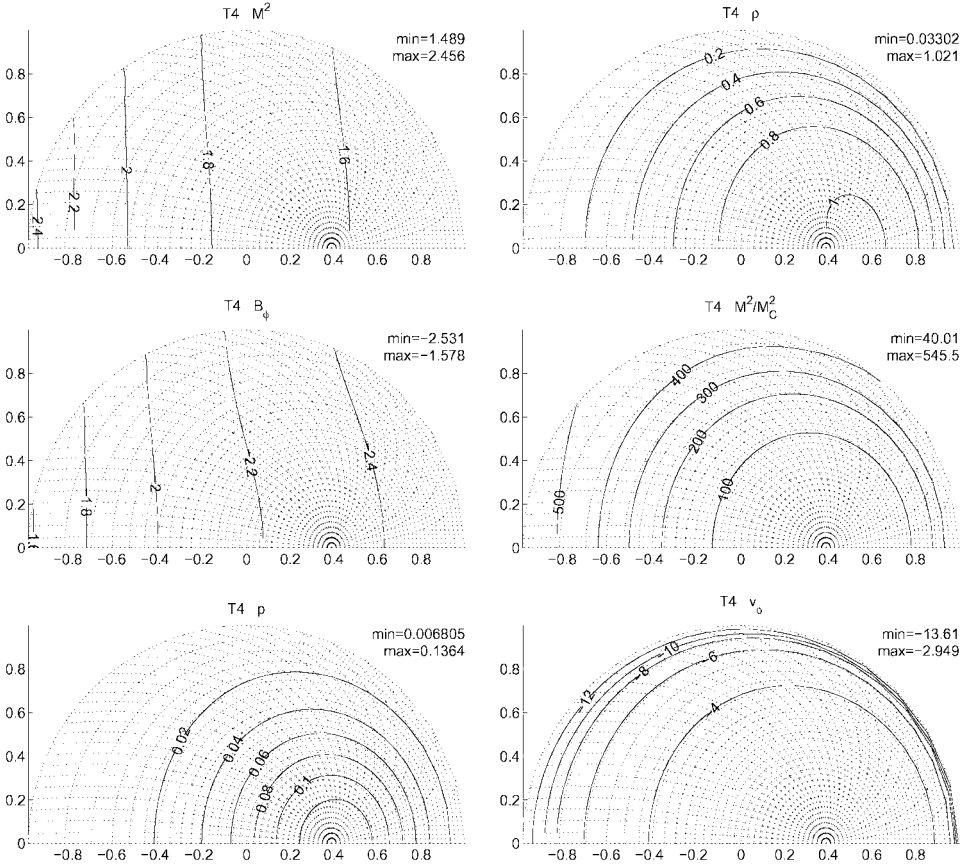
FIG. 12. As in Figs. 7, 9, and 11, for the fast elliptic T4 equilibrium.
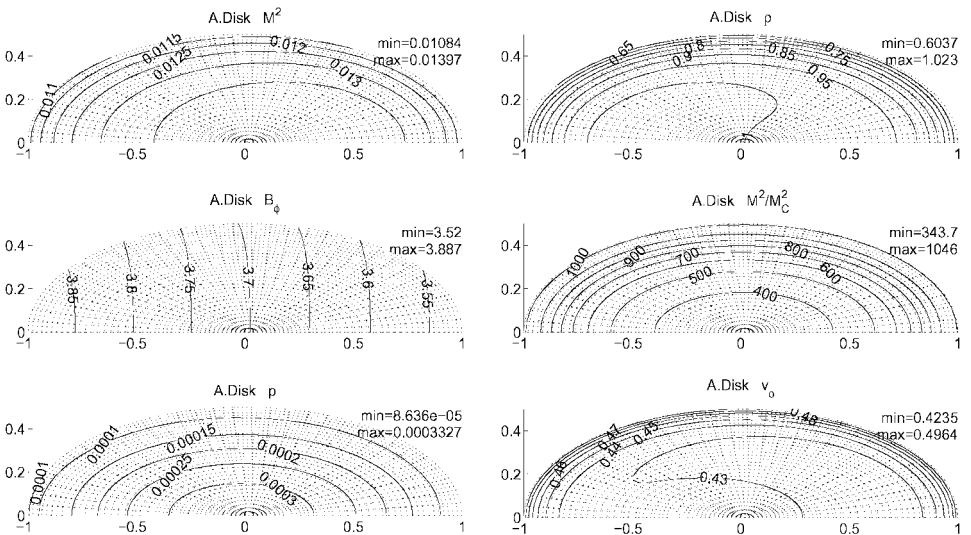

FIG. 13. The accretion disk equilibrium in the same format as Figs. 7, 9, 11, and 12.

PHOENIX can also handle external gravitational fields, we intend to analyze the stability properties of flux tori in accretion disks starting from similar stationary, gravitationally stratified MHD equilibria [4, 8].

4.2. An Open Magnetic Configuration: The Stellar Breeze

Our final astrophysically relevant case considers a stellar wind in a dipolar coronal magnetic field. Specifically, we present a top-down symmetric (w.r.t. the equator) solution around a gravitating star modeled as a subslow elliptic flow equilibrium (SB in Table II) in a spherical annulus geometry. The solution is shown in Fig. 14 and is computed on a 81×81 finite element grid.

The domain we consider extends to five stellar radii ($b/a = 5$ in Eqs. (14) and (15)). On the stellar surface we impose the boundary condition $\psi = \cos^2 \theta$ to get a dipolar magnetic field solution, as seen in the magnetic flux contours in Fig. 14. On the outer radial boundary of the domain we impose the condition that the magnetic field is normal to the boundary.
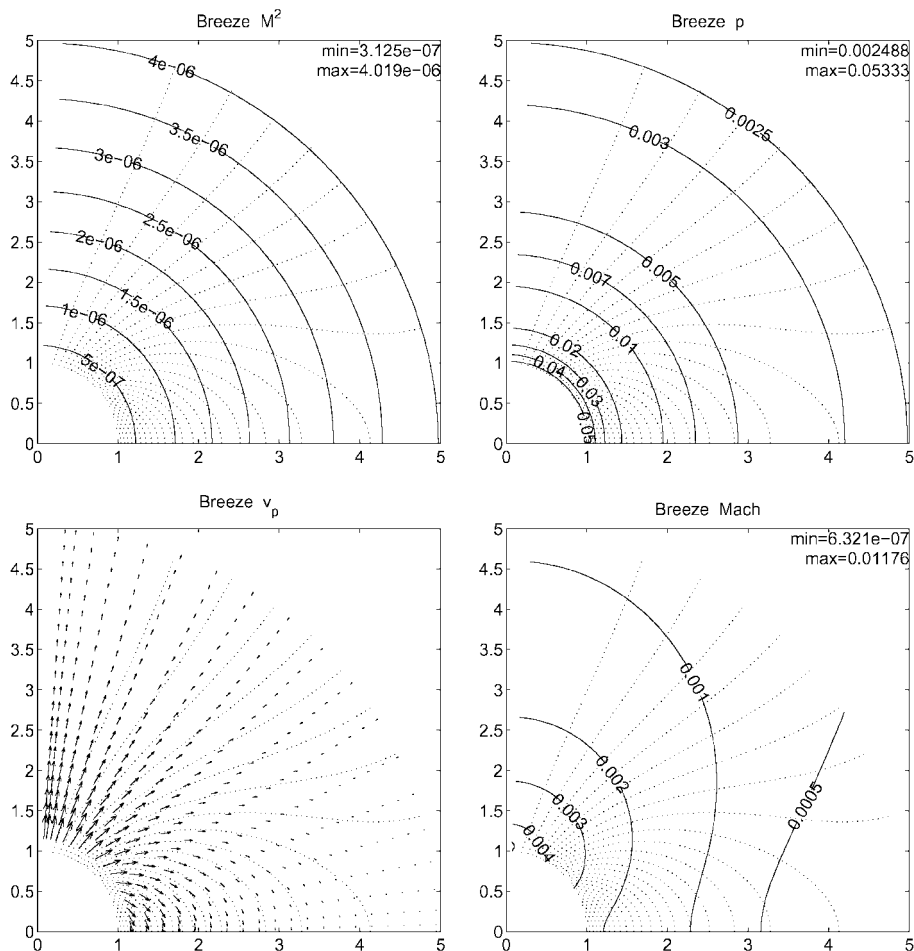

FIG. 14. The stellar breeze equilibrium. (Top left) The squared poloidal Alfvén Mach number M^2 and the poloidal stream function ψ (dotted lines). (Top right) The pressure p superimposed on ψ. (Bottom left) The poloidal flow pattern in the stellar corona. (Bottom right) The Mach number v_p/c_s with $c_s = \sqrt{\gamma p/\rho}$.

Symmetry requirements dictate the other boundary conditions: on the symmetry axis the poloidal magnetic flux is constant and $\psi = 0$ is imposed, while top-down symmetry requires the magnetic field to be normal to the equator.

Regularity on the symmetry axis demands that B_ϕ and v_ϕ vanish on this axis. This is achieved by setting $\lambda_4 = \psi$. The other profiles are taken to be constant: $\lambda_i = 1$, $i = 1, 2, 3, 5$. Hence, we calculate an equilibrium where the entropy is a constant globally. Furthermore, the ratio of specific heats $\gamma = 1.2$.

Since the profiles $\lambda_{1,2,3}$ are all constant and equal to one and $A_3 \ll 1$ (see Table II), the Bernoulli variable P only depends on $r = \sqrt{R^2 + Z^2}$ via the gravitational potential. Consequently, M^2 should only depend on r since for near-static (subslow) equilibria there is a direct relation between P and the poloidal Alfvén Mach number M^2 (see the Appendix). As a result, the poloidal Alfvén Mach number is far from being a flux function. Similarly, pressure and density decrease radially outward in accord with the gravitational stratification. This is clearly seen in Fig. 14. The strength of the gravitational field can again be quantified by the dimensionless ratio $v_{\mathrm{esc}}/c_s = 2.236$ at the stellar surface. Since the outward pressure gradient force is insufficient to accelerate the coronal plasma to supersonic speeds (bottom panels of Fig. 14), the obtained solution can be referred to as a stellar "breeze." It will be of interest to explore parameter regimes expected to result in transonic wind solutions, where FINESSE calculations of the elliptic flow regions can be used to accelerate the solution procedure for obtaining such transonic stationary states [14].

5. CONCLUSIONS

We have presented a new code, FINESSE, for computing stationary axisymmetric MHD equilibria. The presence of flow leads to serious complications in computing equilibria, which in our paper are overcome by reducing the original ideal stationary MHD equations to a compact elegant form. The reduced set of two nonlinear equations, of which one is algebraic and the other is a PDE, is solved accurately by a simple, fast, and effective iterative scheme. The chosen approach allows us to deal with a large variety of fusion and astrophysically relevant plasmas, as demonstrated in the numerical examples. Equilibria delivered by FINESSE are extremely accurate, so that they can readily be used for subsequent spectral analysis.

APPENDIX

The solution procedure to obtain stationary MHD equilibria followed in FINESSE translates the freedom in the five flux functions into problem-specific choices for the unit profiles λ_i and their (relative) amplitudes A_i. Input values for the amplitudes implicitly prescribe some basic physical parameters for the calculated equilibria. As an example, we illustrate this for a general subslow (near-static) equilibrium. Similar arguments can be used to relate values for A_i to physical quantities for slow and fast elliptic solutions.

In a near-static case, we have $M^2 \ll 1$ and $M^2/M_c^2 \ll 1$. Under these conditions, the variable P, as appearing in the Bernoulli equation (32), is directly related to the magnitude of the poloidal Alfvén Mach number:

$$\lim_{M^2/M_c^2 \to 0} \frac{P}{M^{2(\gamma-1)}} = 1. \tag{40}$$

When we take a small value for $A_3 \ll 1$, we can approximate $P \approx A_2\lambda_2(\psi)/\lambda_1(\psi)$ and thus use the input value for A_2 to set the magnitude of M^2 directly (which must be consistent with $M^2 \ll 1$). As a general result, we can conclude from Eq. (40) that M^2 is nearly a flux function in the limit of negligible poloidal flow.

In combination with the condition $M^2 \ll 1$, the condition $A_3 \ll 1$ is equivalent to saying that the nonparallel (to the magnetic field) part of the toroidal velocity component is much smaller than the sound speed. Since the nonparallel toroidal velocity is $R\Omega$, this statement is confirmed by the observation

$$\lim_{M^2 \to 0} \frac{1}{2}(\gamma - 1)\frac{R^2\Omega^2}{c_s^2} = \frac{R^2\Lambda_3}{\Pi_1} = \frac{(1 + \epsilon x)^2 A_3\lambda_3(\psi)}{\lambda_1(\psi) + (1 + \epsilon x)^2 A_3\lambda_3(\psi)} \leq 1, \qquad (41)$$

where $c_s \equiv \sqrt{\gamma p/\rho}$ is the adiabatic sound speed.

The last deterministic input variable is A_4, and we now demonstrate how its value—for preselected A_2 and A_3—determines the toroidal plasma beta $\beta_t \equiv 2p/B_\phi^2$. Indeed, in the no-poloidal flow limit, the variable Q appearing in the Bernoulli Eq. (32) is directly related to the magnitude of the poloidal Alfvén Mach number and the toroidal plasma beta, viz.,

$$\lim_{M^2/M_c^2 \to 0} QM^2 = \frac{\gamma - 1}{\gamma}\frac{1}{\beta_t}. \qquad (42)$$

Therefore, provided $A_4/\epsilon \gg 1$, the toroidal plasma beta is a flux function to lowest order in the inverse aspect ratio ϵ:

$$\lim_{\epsilon \to 0} \frac{\beta_t}{\epsilon^2} = \frac{\gamma - 1}{\gamma}\frac{\lambda_1^{\gamma/(\gamma-1)}}{A_2^{1/(\gamma-1)}A_3 A_4^2\lambda_2^{1/(\gamma-1)}\lambda_3\lambda_4^2}. \qquad (43)$$

With amplitudes A_2 and A_3 given, this relates the magnitude of β_t to amplitude A_4.

REFERENCES

1. A. J. C. Beliën, S. Poedts, and J. P. Goedbloed, Two-dimensional equilibrium in coronal magnetostatic flux tubes: An accurate equilibrium solver, *Comput. Phys. Commun.* **106**, 21 (1997).

2. A. J. C. Beliën, J. P. Goedbloed, and B. van der Holst, Axisymmetric plasma equilibria with flow: A new solver, *Europhy. Conf. Abstr.* **24B**, p. 892 (2000).

3. A. J. C. Beliën, M. A. Botchev, J. P. Goedbloed, B. van der Holst, and R. Keppens, Influence of poloidal flow on TAE modes, in *Proceedings of 28th EPS conference on controlled fusion and plasma physics, June 18–22, 2001, Funchal Portugal* (2001), Paper P3.041. Europhys. Conf. Abstr. 25A p. 1077 (2001).

4. A. J. C. Beliën, J. P. Goedbloed, and B. van der Holst, MHD waves and instabilities in accretion discs, in *Proceedings of 28th EPS conference on controlled fusion and plasma physics, June 18–22, 2001, Funchal, Portugal* (2001), Paper P3.110.

5. A. Bondeson, G. Vlad, and H. Lütjens, Resistive toroidal stability of internal kink modes in circular and shaped tokamaks, *Phys. Fluids* **7**, 1889 (1992). Europhys. Conf. Abstr. 25A p. 1309 (2001).

6. J. P. Goedbloed, Some remarks on computing axisymmetric equilibria, *Comput. Phys. Commun.* **31**, 123 (1984).

7. J. P. Goedbloed and A. Lifschitz, Stationary symmetric magnetohydrodynamic flows, *Phys. Plasmas* **4**, 3544 (1997).

8. J. P. Goedbloed, Transonic magnetohydrodynamic flows in laboratory and astrophysical plasmas, *Phys. Scripta* **T98**, 43 (2002).

9. J. P. Goedbloed and A. Lifschitz, submitted for publication.

10. E. Hameiri, The equilibrium and stability of rotating plasmas, *Phys. Fluids* **26**, 230 (1983).

11. B. van der Holst, A. J. C. Beliën, and J. P. Goedbloed, Low frequency Alfvén waves induced by toroidal flows, *Phys. Plasmas* **7**, 4208 (2000).

12. G. T. A. Huysmans, J. P. Goedbloed, and W. Kerner, Isoparametric bicubic Hermite elements for solution of the Grad-Shafranov equation, in *Proc. CP90 Conf. on Comp. Phys. Proc.* (World Scientific Publ. Co. 1991), p. 371.

13. G. T. A. Huysmans, J. P. Goedbloed, and W. Kerner, Free boundary resistive modes in tokamaks, *Phys. Fluids* **5**, 1545 (1993).

14. R. Keppens and J. P. Goedbloed, Numerical simulations of stellar winds: polytropic models, *Astron. Astrophys.* **343**, 251 (1999).

15. W. Kerner, J. P. Goedbloed, G. T. A. Huysmans, S. Poedts, and E. Schwarz, CASTOR: Normal-mode analysis of resistive MHD plasmas, *J. Comput. Phys.* **142**, 271 (1998).

16. H. Lütjens, A. Bondeson, and A. Roy, Axisymmetric MHD equilibrium solver with bicubic Hermite elements, *Comput. Phys. Commun.* **69**, 287 (1992).

17. K. G. Powell, P. L. Roe, T. J. Linde, T. I. Gombosi, and D. L. De Zeeuw, A solution-adaptive upwind scheme for ideal magnetohydrodynamics, *J. Comput. Phys.* **154**, 284 (1999).

18. W. H. Press, B. P. Flannery, S. A. Teukolsky, and W. T. Vettering, *Numerical Recipes* (Cambridge Univ. Press, New York, 1989).

19. G. Strang and G. J. Fix, *An Analysis of the Finite Element Method* (Prentice Hall, Englewood Cliffs, NJ, 1973).

20. G. Tóth, R. Keppens, and M. A. Botchev, Implicit and semi-implicit schemes in the versatile advection code: numerical tests, *Astron. Astrophys.* **332**, 1159 (1998).

21. G. Vlad, H. Lütjens, and A. Bondeson, Free boundary toroidal stability of ideal and resistive internal kinks, in *Controlled Fusion and Plasma Heating, Proc. 18th European Conf.* (EPS, Geneva, 1991), Vol. 15C, Part IV, p. 85.

22. R. Żelazny, R. Stankiewicz, A. Galkowski, and S. Potempski, Solutions to the flow equilibrium problem in elliptic regions, *Plasma Phys. Control. Fusion* **35**, 1215 (1993).

23. H. P. Zehrfeld and B. J. Green, stationary toroidal Equilibria at finite beta, *Nucl. Fusion* **12**, 569 (1972).